

User-Intended Doppler Measurement Type Prediction Combining CNNs With Smart Post-Processing

Andrew Gilbert, *Student Member, IEEE*, Marit Holden, Line Eikvil, Mariia Rakhmail, Aleksandar Babić, Svein Arne Aase, Eigil Samset, Kristin McLeod

Abstract— Spectral Doppler measurements are an important part of the standard echocardiographic examination. These measurements give insight into myocardial motion and blood flow providing clinicians with parameters for diagnostic decision making. Many of these measurements are performed automatically with high accuracy, increasing the efficiency of the diagnostic pipeline. However, full automation is not yet available because the user must manually select which measurement should be performed on each image. In this work, we develop a pipeline based on convolutional neural networks (CNNs) to automatically classify the measurement type from cardiac Doppler scans. We show how the multi-modal information in each spectral Doppler recording can be combined using a meta parameter post-processing mapping scheme and heatmaps to encode coordinate locations. Additionally, we experiment with several architectures to examine the tradeoff between accuracy, speed, and memory usage for resource-constrained environments. Finally, we propose a confidence metric using the values in the last fully connected layer of the network and show that our confidence metric can prevent many misclassifications. Our algorithm enables a fully automatic pipeline from acquisition to Doppler spectrum measurements. We achieve 96% accuracy on a test set drawn from a separate clinical site, indicating that the proposed method is suitable for clinical adoption.

Index Terms— Convolutional neural network (CNN), deep learning, classification, ultrasound (US)

I. INTRODUCTION

ECHOCARDIOGRAPHY is the primary method used to image the heart due to its portability, affordability, and

Manuscript received May 31, 2019 and revised November 5, 2019. This project has received funding from the European Union's Horizon 2020 research and innovation program under the Marie Skłodowska-Curie grant agreement No 764738.

A. Gilbert and E. Samset are with GE Healthcare and also with the Department of Informatics at the University of Oslo, both Oslo, NO (email: andrew.gilbert@ge.com; eigil.samset@ge.com).

M. Holden and L. Eikvil are with the Norwegian Computing Center, Oslo, NO (email: marit.holden@nr.no; line.eikvil@nr.no).

A. Babić was with GE Healthcare in Oslo, NO for his contribution to this work (email: aleksandar.babic@gmail.com).

M. Rakhmail, S. A. Aase, and K. McLeod are with GE Healthcare in Kharkiv, UA; Trondheim, NO; and Oslo, NO respectively (email: mariya.rakhmail@gmail.com; sveinarne.aase@gmail.com; and kristin.mcleod@gmail.com).

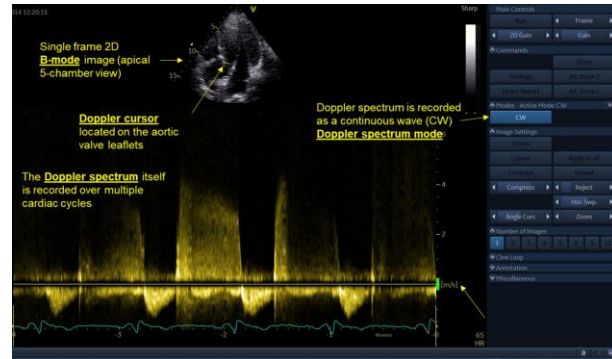


Fig. 1. Example of a doppler acquisition shown on EchoPAC (GE Healthcare, Horten, NO) depicting the relevant information to a spectrum classification problem as a clinician would see it.

absence of ionizing radiation. The diagnostic power of echocardiography is reflected in clinical guidelines, with echocardiography indices included as both minor and major clinical diagnostic criteria in many protocols [1]. As computational power increases, image quality improves, and consequently, the theoretical accuracy of clinical measurements also increases.

In addition to the diagnostic power, there is a growing trend to use echocardiography as a therapy guidance tool to support interventions and complement other imaging modalities. Minimally invasive valve interventions are much less risky than full surgery and are becoming the therapy of choice as techniques and prosthetics advance. Spectral Doppler imaging is the primary method to assess blood flow across valves, a crucial step for intervention planning and follow-up [2]. Therefore, spectral Doppler imaging has become an integral component of the echocardiography exam to provide a means to assess hemodynamic function in all four valves of the heart.

A. Spectral Doppler Measurements

Fig. 1 shows an example of a spectral Doppler acquisition as seen in EchoPAC (GE Healthcare, Horten, NO). There are many important features of the acquisition that are available within the raw data of each recording:

- The **Doppler spectrum** is displayed over multiple cardiac cycles for analysis and measurement.

- The **relative baseline** of the Doppler spectrum can be adjusted by the user during acquisition to focus on a specific part of the spectrum and prevent aliasing.
- The **mode** provides information on how the Doppler spectrum was acquired. Spectral Doppler incorporates three main imaging modes: continuous wave (CW) Doppler, pulsed wave (PW) Doppler, and tissue velocity Doppler (TVD). CW is used to measure high velocity blood flow across valves, PW provides flow analysis at specific spatial points, and TVD provides quantifiable myocardial velocities.
- The 2D **B-mode** (brightness mode) image shows the orientation of the probe with respect to the physical anatomy of the heart. Doppler spectra can be obtained from a variety of probe positions and angles depending on the desired measurement. The scan converted B-mode image is displayed here to orient the user.
- The **Doppler cursor**, visible on top of the B-mode image, indicates from where in anatomical space the spectrum was extracted. This parameter is interpreted in the context of the B-mode image. See Fig. 2 for a visual overview of how the cursor location corresponds to specific points in anatomical space. In the TVD classes the cursor is focused directly on the tissue, while in the CW and PW classes the cursor is focused on an area of blood flow. Exact positioning will depend on the desired measurement, operator preference, and individual patient anatomy.

Together, this collective information identifies the type of Doppler spectrum and therefore which measurements should be performed.

B. Clinical Need for Measurement Type Classification

Accurate automatic classification of Doppler measurement types can be combined with already available automated measurement techniques (e.g. [3], [4]) to provide fully automated analysis of Doppler spectra. This can increase the efficiency of workflow, allowing clinicians to spend more time on difficult measurements.

Furthermore, many clinics have petabytes of patient data in their archive systems from tracking patients over time. Thus, if used in combination with automated measurement techniques, one application of automatic Doppler measurement type classification is to perform rapid historical analysis on past exams in a robust and standardized manner. All information used in our classification system is readily available in hospital archives if those archives store the raw data for each patient. Knowing a patient's progression from previous checkpoints can provide further information to support therapy planning. Therefore, historical analysis would provide clinical value through objective study of measurements over time. Another application is continually performing analysis on patients, which could bring statistical power to the development and augmentation of clinical guidelines.

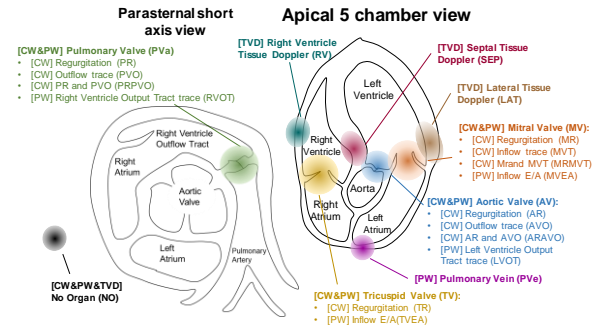


Fig. 2. Each of the Doppler measurement types sorted by the location of the cursor position. Each color corresponds to a different region in anatomical space. The mode of each measurement is shown in front. Apical 5 chamber and parasternal short axis views are shown here for illustrative purposes only, to demonstrate the relative positions of the classes. Doppler spectra are typically acquired from a variety of echocardiographic views and part of the challenge of this problem is that the spatial relationship between structures demonstrated above will change depending on the view used for image acquisition. The No Organ (NO) class refers to images of air and ultrasound gel.

C. Related Work

1) Ultrasound Classification

Doppler measurement type classification is unique because of the heterogeneity of data available in each classification example. As shown in Fig. 1, each recording contains image data, spectral data, modal parameters, a baseline position, and Doppler cursor coordinate locations. Previously, many of these items have been automatically classified individually, borrowing techniques from non-medical domains. Processing of spectral data has been a common task for several decades in speech recognition [5], and these techniques have been applied to Doppler spectra as well. For example, Wright *et al.* used artificial neural networks to classify Doppler spectra from arteries [6]. Meanwhile, automatic image classification has also become increasingly common as CNNs have surpassed the accuracy of humans on many tasks. Recently, these techniques were applied to echocardiographic B-mode images to automatically classify cardiac views with very good results [7], [8].

2) Multi-modal Learning

In non-medical fields, several groups have also looked at how data from different modalities can be combined. Ngiam *et al.* showed how a deep autoencoder could be trained with both video and speech data to generate a shared representation [9]. Ephrat *et al.* demonstrated how video and speech data could be encoded separately and then combined in a bidirectional long short-term memory network to solve the cocktail party problem of singling out a single speaker in a noisy audio track [10].

While many deep learning techniques have successfully made the transition from non-medical to medical applications

[11], applying multimodal learning techniques remains a challenge because there are several orders of magnitude difference in the amount of data available. For example, Ephrat *et al.* were able to use >2000 hours of automatically annotated data. The annotation of such a volume of data in the context of Doppler spectra is challenging due to the lack of available simulated data. Transfer learning and fine tuning have

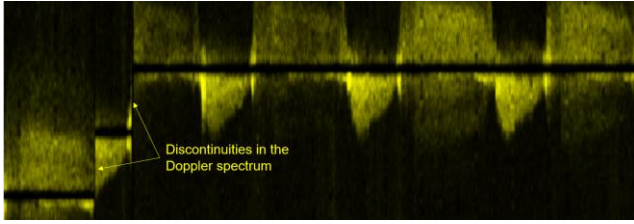


Fig. 3. Discontinuities arise when the operator shifts the baseline during acquisition. This is common practice when acquiring several measurements.

previously been applied to solve data magnitude problems in medical imaging [12]. However, it is of limited use here since task objectives are different, and the relationship between the modalities (Doppler spectrum to B-mode) varies for each Doppler measurement class.

3) Confidence

One challenge in ultrasound imaging is that images acquired in clinical settings are not necessarily in standard views. This is a concern in the given classification problem where misclassifications can be costly, and the model is exposed to only a subset of possible views that might be seen in a clinical workflow. Therefore, an algorithm to classify such images needs a mechanism to handle non-standard cases. This can be either collecting large data-sets that can cover all possible views (even those that are non-standard) or a mechanism to bail-out when the image doesn't fall in the label set, such as via confidence metrics with a set threshold for acceptance.

Several groups have looked at how networks can give a prediction of confidence along with an output label. It is well known that CNNs are prone to overfitting and cannot generalize well from the training set to unseen inputs [13]. Previously, Bayesian models have been used to provide a better estimate of model uncertainty by encoding model weights as a probability distribution, but often come with increased parameter count and a higher computational cost to adequately model random distributions [14]. Monte Carlo dropout (MC-dropout) is one method to approximate Bayesian inference with a lower computation cost by using dropout at test time [15]. Other methods such as temperature scaling [16] or histogram binning [17] calibrate fully trained network outputs without changing inference. Parameters are learned on the validation set to map network outputs to a true confidence distribution. These methods have the advantage of maintaining inference time and increasing the interpretability of the results without sacrificing a loss in the accuracy of the model.

D. Contributions

After an analysis of the data, we eliminated the spectral information from our processing pipeline. This reduced our input to a B-mode image, Doppler cursor coordinate location, baseline position, and mode parameter. Although spectra provide useful information (and are used by clinical experts when labelling images), there are many variations in the collection of spectra that make it difficult to use in a network. For example, as shown in Fig. 3, spectral data can have discontinuities in the baseline as the user changes the

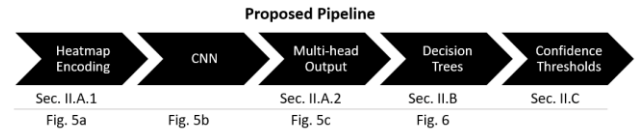


Fig. 4. The pipeline of the proposed method with relevant section and figure numbers for full details.

parameters during acquisition. Spectral data is also variable length, which effectively shrinks or expands the features in the output image. Dealing with variable length would require an even larger dataset, since CNNs are not magnitude invariant. To avoid adding unnecessary complexity, we developed a method that does not rely on spectral data, and instead, focused on the integration of the latter four parameters in our classification. We can eliminate the spectra from our method because we develop a novel pipeline which breaks the problem into a series of simpler pieces, and we create an alternate way of uniquely identifying the spectra using these pieces. Our pipeline is outlined in Fig. 4 with references to the relevant figure and section numbers for each piece. In brief, the principle contributions of our pipeline are four-fold:

(1) **Heatmap encoding:** We show how to encode spatial features at the input of CNNs, when multi-modal data includes coordinate locations as features.

(2) **Multi-head output:** We borrow techniques from multi-task learning to develop a multi-head learning strategy that integrates mode information to prevent misclassifications and reduce network size.

(3) **Decision tree mapping:** We use decision trees to incorporate user-defined imaging parameters in order to simplify the task of the CNN and better predict user intentions for the desired measurement type.

(4) **Confidence Thresholds:** We demonstrate how neural network layers, besides just the final layer, can be used to define a confidence metric that will disregard many images that differ from the training set. Our method requires no extra trained parameters, uses a fully nonlinear mapping between the output values and the network confidence estimate, and can be dynamically modified at inference time depending on the desired tradeoff between ignored and error rates.

To the best of our knowledge, this is the first work to use CNNs to classify Doppler measurement types. We achieve high accuracy on the task, while maintaining a small memory footprint and close to real-time performance. Moreover, several of the methods developed in this work may be applicable to other classification problems, especially in medical imaging.

II. METHODS

Through conversations with clinical experts, we identified 18 of the most common measurement classes for adults. Three additional types of Doppler measurements do exist, but these are infrequent in clinical practice and are thus excluded from the current network design. We take two steps to account for measurement types not covered in our label set. First, to avoid making a classification on images scanned without a visible B-

mode image on screen, a no organ (NO) class was added which consisted only of images where air and varying amounts of ultrasound gel were scanned. The Doppler cursor, baseline, and other parameters were chosen to cover a variety of possible inputs for the NO images. Second, we design a confidence metric in Sec. II.C to discard images from other classes. A full discussion of each of the measurement types is outside the scope of this work, but Fig. 2 shows a diagram of the relative cursor positions as well as the acronyms for each type. An outline of each measurement’s use and acquisition is available in [1], and reports specific to CW and PW [18], and TVD [19] mode measurements are also available.

The proposed method performs a classification on these Doppler measurement types. Our method first classifies the relevant anatomical region using a CNN as described in Sec. II.A. Sec. II.A.1 explains heatmap encoding at the input of the network while Sec. II.A.2 describes a multi-head output approach to divide the classification according to the imaging mode. A decision tree to simplify the network’s classification task is presented in Sec. II.B. A confidence metric is defined in Sec. II.C to avoid misclassifications in the case of low-confidence cases such as for images that fall outside of our class set or images with poor quality. Finally, the design of the dataset used for training and testing is outlined in Sec. II.D.

A. Determining Cursor Location with CNNs

As shown in Fig. 1, a single Doppler recording is composed of many multi-modal features. Given the information in the format of Fig. 1, an expert observer can easily integrate the relevant information and classify the type of measurement that should be made. However, it would be unrealistic to expect a network to perform a classification given only an image such as Fig. 1, because some of the most important pieces of information are not emphasized in the image. For example, the Doppler cursor is very important to the classification because it indicates the location of the Doppler spectrum within the heart, but it is only a small marker on the image.

Instead, we extract all the relevant data individually from each recording. The mode is recorded as either CW, PW, or TVD. The relative baseline is extracted as a float in the range from 0 to 1, where the default (unchanged) location is 0.5. The raw B-mode data is extracted as a 512x256 image, since the depth dimension is usually much larger in the raw data. Note that the non-scan converted (beam space) data is used directly rather than the scan-converted (probe space) data that is shown to the user. The added step in the pipeline to scan-convert the images yields no gain in this application where the Doppler cursor position relative to the heart structures is the key piece of information.

As shown by the different colors in Fig. 2, the measurement types can be grouped into 9 locations in anatomical space. Since the relationship between cursor coordinates and image features would be similar for each of these locations, we merge all measurements from the same anatomical location into the same class for the CNN. Thus, the task of the CNN is only to figure out which anatomical location the measurement came from, the rest is handled during post-processing as described in Sec. II.B. The only inputs into the network are the B-mode image and the cursor coordinate.

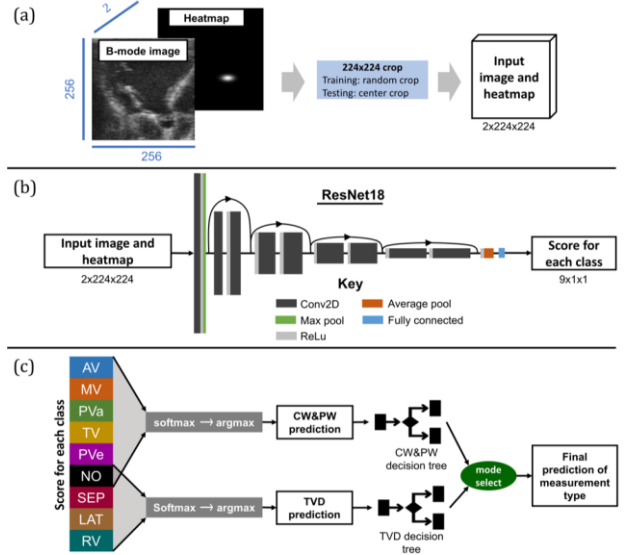


Fig. 5. (a) Network input for our spectrum classification. The heatmap of the Doppler cursor location is appended as a channel to the non-scanconverted B-mode image and both are cropped to 224x224 before being input to the network. (b) We primarily used a ResNet18 architecture to classify the images although we do experiment with other network architectures (section III.A.3). For full details of ResNet18 see Zhang *et al.* [24]. (c) The last fully connected layer (of size 9) is split into two groups. The No Organ (NO) class is input to both groups so the CW&PW node is size 6 and TVD node is size 4. Each group is passed to its own softmax classifier, argmax and decision tree (see Fig. 6 for decision trees). The mode parameter is used to select between the two outputs to yield a final class. See Fig. 2 for class abbreviations.

1) Heatmap Encoding

The position of the cursor is extracted relative to the original B-mode image as a coordinate pair, but Liu *et al.* showed CNN’s are typically poor at learning mapping between coordinates in cartesian coordinate space and pixel space [20]. However, in landmark detection problems, networks are able to generate heatmaps of likely locations with high accuracy [21]. Intuitively this makes sense, since there is a one-to-one mapping from the coordinate space of the input image to the output heatmap. Logically, networks should also perform better if landmarks at the input are encoded as heatmaps instead of input as coordinates. To encode our Doppler cursor location as a heatmap, we generate a 2D normal gaussian probability density function with a standard deviation of 10 pixels centered at the cursor coordinate. The heatmap is generated in 512x256 resolution to match the original raw data, and then appended to the input image as an additional channel before rescaling both to 256x256. This has the effect of compressing the gaussian vertically, which allows the expected spatial distribution of the landmark to more closely match the physical dimensions of the raw data. An example heatmap is shown in Fig. 5a. Finally, we cropped both image and heatmap to 224x224. During training we used random crops for augmentation, and during validation and testing we used center crops.

2) Multi-Head Network

As shown in Fig. 2, other than Pulmonary Vein, the CW and PW mode measurements share the same anatomical locations. The CW and PW locations are also completely distinct from the TVD mode measurements (except for the no-organ synthetic

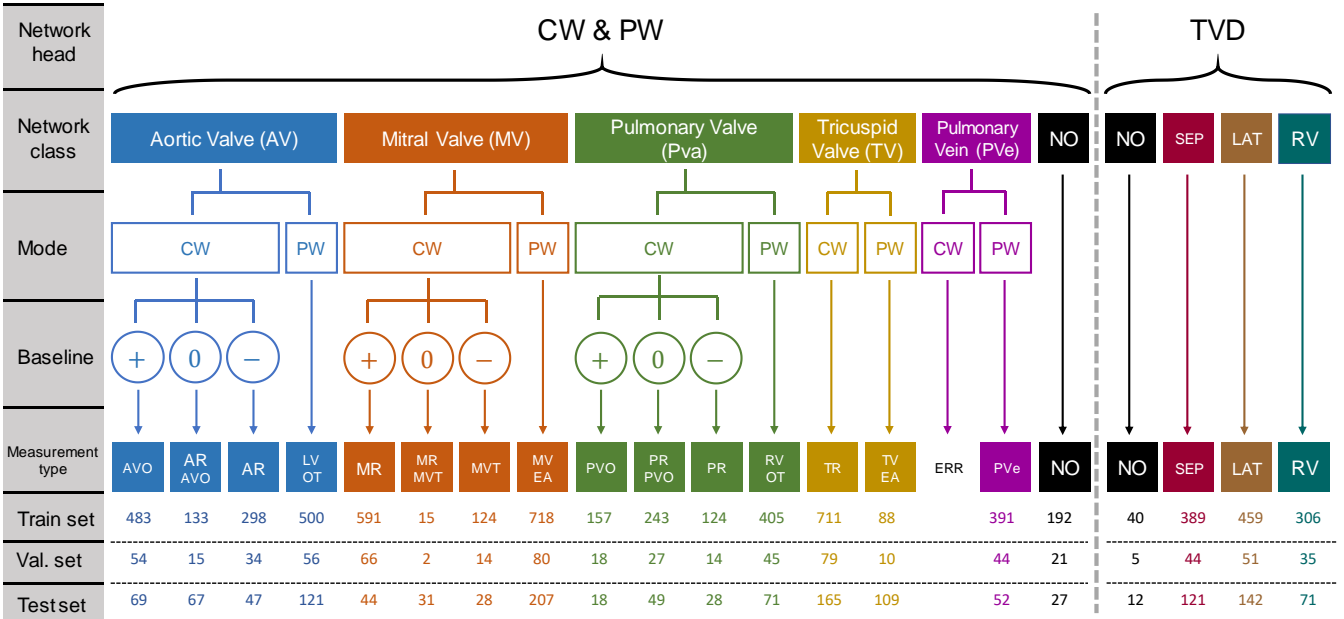


Fig.6. Decision trees from the classes output by the network to the final classes determining the measurement type. The network has two heads, the CW&PW head and the TVD head. Outputs from each head are mapped to final classes using the mode and baseline parameters and then the mode is used to decide between the CW&PW head output and the TVD head output (Fig. 5c). For the baseline: (-) indicates a baseline in the range [0, 0.5], (0) indicates a baseline at 0.5 and (+) indicates the range (0.5, 1]. If nothing is indicated for mode or baseline, then those parameters are not used for that mapping (all values map to the same class). For example, every image in the TVD head is guaranteed to be mode TVD so the mode is not used in this head. Training, validation, and test set sizes are shown below each class. See Fig. 2 for locations of each class and acronym definition. ARAVO, MRMVT, and PRPVO are combinations of AR/AVO, MR/MVT, and PR/PVO respectively.

class). Because the mode parameter is always set by the user, simply training a network to classify all outputs would lead to unnecessary errors. For example, the network should never classify an RV image (TVD mode) as an LVOT (PW mode), but without explicitly separating these modes this misclassification may occur. To solve this, the mode parameter could be used to linearly split our set of anatomical location classes into unique sets, one for CW&PW and one for TVD. One approach would then be to train a different network for each mode and call the network for the relevant mode during inference. However, this approach doubles the memory footprint of any implementation, which is a downside for integration into a resource-constrained environment.

An alternative solution is to frame this as a multi-task learning problem. Multi-task learning integrates the information from several related tasks into a single network by implementing a separate softmax classifier (or classification “head”) for each task. Often in multi-task networks, information from one task improves performance on another and the approach has proven to be successful in a variety of deep learning applications [22]. Our method is slightly different from a multi-task approach because although there are multiple outputs, only one is relevant to the given input. In detail, whereas in multi-task learning loss can be taken from both heads during training, we backpropagate loss only from the head with a mode matching that sample. During inference, the CNN yields predictions from both heads, but only the value from the relevant mode is read by the calling function. Due to these differences we instead call this a “multi-head” network.

Input to each classification head are the values from the last fully connected layer for the classes that belong to that mode. With this design choice, we exploit the information about the

different modes by including separate heads and loss functions for the CW&PW and TVD groupings of anatomical locations. The architecture of our multi-head network is shown in Fig. 5c.

B. Decision Tree Mapping

After finding the anatomical location with the CNN, the next step in the pipeline is determining the final measurement type. The mode and relative baseline position parameters extracted from the spectrum linearly separate the measurement types in each anatomical region because users change those parameters based on which type of measurement they wish to acquire. Therefore we can use post-processing decision trees from each head. The decision trees from each head are shown in Fig. 6. One possible error is introduced in this scheme when a CW image is classified as a Pulmonary Vein (PVe). In preliminary experiments this was never an issue, but occurrence in a clinical setting would require manual re-classification.

Decision trees are a better solution than feeding the parameters into the network because it avoids unnecessary mistakes and enables the CNN to use classes that are based solely on regions in anatomical space. Otherwise, the CNN would likely be confused between classes from the same anatomical region. Additionally, grouping the classes increases the training and test set sizes for all classes. This is an important consideration since several of the original smaller classes did not have enough images for a network to properly converge.

C. Confidence Metric

Correct classifications from the network will yield significant time savings for clinical users by automatically launching the tool associated with that Doppler measurement

type, where available. However, incorrect classification comes with a cost, as the user will then have to navigate back in the menu and select the correct measurement type. As automation continues to permeate clinical workflows, this cost may become larger as an initial misclassification could trigger unrelated measurements and automated tools. Moreover, there may be images in a clinical setting that are different from those seen during training. Thus, it is important for the network to have a bail-out mechanism on images with high uncertainty.

In our approach, we use the last fully connected layer before the softmax classifier, named the “pre-softmax” layer. This layer was chosen because we could easily extract raw network estimates for all classes before they were distorted by the multiple heads. The output of the pre-softmax layer for each example in the training set is recorded after the network weights are trained and frozen. The training set is used because the validation set is not large enough to provide statistical significance. The recorded values are divided into quantiles. That is, rather than learning a mapping from outputs to true confidence (as was done in [16] and [17]), we find a series of cutoff values for each confidence level. During test time, the quantile is set based on the desired tradeoff between error rate and ignored rate. The maximum output value is found as usual, but if the pre-softmax value for that class falls below the given threshold then the image is labeled as low confidence and ignored.

D. Dataset

The training and validation datasets consisted of exams previously collected by GE Healthcare for internal tool development. All exams were fully anonymized and came from a variety of clinical sites. Exams were collected to try to maintain a high number in each class, but more images were available for classes that occur more frequently in clinical practice (e.g. MV) than those that occur infrequently (e.g. RV). Thus, our dataset is slightly unbalanced because it reflects the clinical distribution of the data. The final set was 7081 images where individual class sizes are shown in Fig. 6. The images were split 90% into training and 10% into validation for each class.

The test set was collected from two institutions that did not have any exams in the training dataset. This was done for two reasons. First, since images are fully anonymized, it is impossible to guarantee that two images from the same institution are not from the same patient. It is crucial for accurate test statistics that the training and test sets contain unique patients. Second, every institution has slightly different acquisition practices and patient populations leading to small differences in the distribution of the images. Thus, to get a result that reflects real performance “in-the-wild” it is important to test on data from a separate institution. The test set contained 1479 images and class distributions are also shown in Fig. 6. All images were labeled by a clinical expert experienced in Doppler spectrum analysis and reviewed for accuracy by two other experts. Roles were swapped between sets, so a different expert did the initial labeling for the test set than the training and validation set.

While gathering the training and validation sets, there were

#	Architecture	Input	Networks	Classification Heads	Accuracy	Size (MB)	Time (ms)
E1	ResNet18	I	2	One head per network	67.1 %	1520	3.96
E2	ResNet18	I + H	2	One head per network	96.8 %	1734	3.82
E3	ResNet18	I + H	1	One head	93.8 %	872	3.93
E4	ResNet18	I + H	1	Training: one head Testing: two heads	96.2 %	847	3.83
E5	ResNet18	I + H	1	Two heads	96.2 %	848	4.07
E6	ResNet34	I + H	1	Two heads	96.2 %	993	7.03
E7	ResNet50	I + H	1	Two heads	95.8 %	1048	9.90
E8	SqueezeNet	I + H	1	Two heads	94.6 %	764	3.92
E9	MobileNetV2	I + H	1	Two heads	94.2 %	699	8.44

Table 1. Comparison of experimental results. In the Input column, I means just the image and I + H means the image with heatmap concatenated as shown in Fig. 5a. In the Classification heads column “one head” refers to a single softmax classifier with all classes, and “two heads” refers to the multi-head approach detailed in Fig. 5c. Memory size and inference time estimates were implemented following [23].

298 images that had insufficient image quality for an expert to classify them. These images were categorized as the *unknown* set to analyze the confidence metric. Additionally, 30 images were identified that belonged to the three measurement classes not included in this network because they appear infrequently in clinical practice. These images were put into the *extra* set to analyze the confidence metric.

III. RESULTS

A. Cursor Location with CNNs

To evaluate the effects of our design decisions, we constructed a series of experiments with results on the test set shown in Table 1.

1) Heatmap Encoding

First, we evaluated the effect of adding the cursor heatmap. We trained using only the B-mode image as an input (E1 in Table 1) and then trained with the cursor heatmap appended to the B-mode image (E2 in Table 1). In both cases, separate networks were trained for each mode (CW&PW vs. TVD). Both experiments used a ResNet18 network (architecture shown in Fig. 5b) [24]. The ResNet architecture was chosen because it achieved high accuracy on a variety of classification tasks. Specifically, ResNet18 has a smaller footprint than other networks and less parameters, which helps avoid overfitting on data-limited tasks. As expected, results showed a significant improvement when the heatmap was included, with overall classification accuracy increasing from 67.1% for E1 to 96.8% in E2.

2) Multi-head Networks

Second, we tested the effect of the multi-head approach. As a baseline approach we trained one network with a single classification head on all 9 classes (E3 in Table 1). There are 9 classes instead of 10 here because with a single classification head only one NO class is needed. Results showed a significant drop in accuracy compared to E2, indicating that the network is not able to fully detect the mode by itself. However, the memory footprint was also cut in half. Our goal was to use the multi-head approach to obtain a network with the same accuracy as two separate networks (E2), but the memory footprint of a single network (E3). To test this, we took the network trained in E3 and applied the multi-head architecture at test time (E4 in Table 1). Next, we tried a single network using the multi-head approach during both training and testing

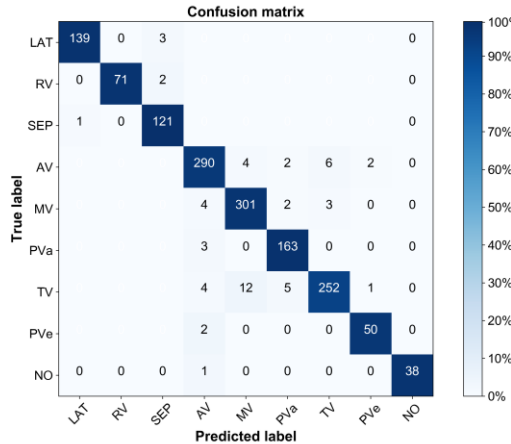


Fig. 7. Confusion matrix on the final test set using the ResNet18 multi-head approach. The boxes where no number is shown will never be misclassified because separate classification heads are used. Colors are normalized to class size (percentages).

(E5). Experiments E2 - E5 all used the same input information, but with different methods of integrating the mode information.

Results showed equivalent performance (96.2%) for E4 and E5, indicating that the multi-head architecture is only important during inference. E4 and E5 both performed significantly better than the single network (E3), and almost as well as the double network approach (E2). This was somewhat surprising, since E5 consistently obtained the better results than E2 on the validation set, but the multi-head approach was still able to achieve similar results with half of the memory footprint. The memory savings make up for the small loss in accuracy for our application and justify the use of the multi-head network.

3) Network Architecture

Third, we tested how results would change with the chosen network size. To test if deeper networks would increase accuracy, we used larger versions of ResNet: ResNet34 (E6) and ResNet50 (E7). To test if similar accuracy could be maintained with a smaller network, we used SqueezeNet (E8) and MobileNetV2 (E9). SqueezeNet [25] and MobileNetV2 [26] are networks designed for high performance on classification tasks in resource-constrained environments. E5-E9 all used the same experimental setup (heatmap encoding and multi-head output) with different network architectures.

Results showed that ResNet34 maintained similar results, while there was a small decrease when moving to ResNet50. Additionally, the memory footprint and inference time increased with these architectures. This indicates that deeper networks may overfit to the smaller dataset used here and come with increased memory size and inference time. There was some performance degradation when using SqueezeNet (94.6%) and MobileNetV2 (94.2%) indicating that these networks do not have the capacity to learn this problem as well as ResNet18. There were slight memory savings with these networks, but not enough to justify the performance drop.

Overall, the optimal approach for implementation considering accuracy, speed, and network size was the ResNet18 multi-head approach (E4 or E5 – results were almost identical between the two). The confusion matrix on the test set

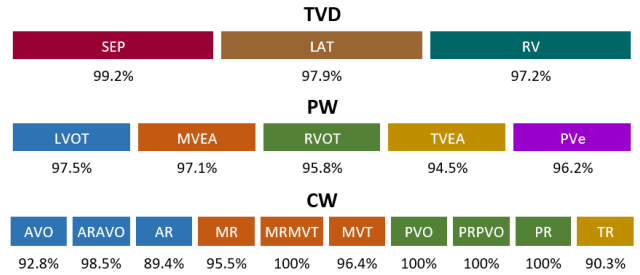


Table 2. Classification accuracy for each measurement type sorted by mode

for E5 is shown in Fig. 7. Tricuspid Valve was the lowest accuracy class with 91%, while all other classes were over 95%.

B. Decision Tree Mapping

Using the decision tree presented in Fig. 6 we mapped the output of the network to the final measurement type classes. The accuracy for each class is shown in Table 2. For the two classes with the lowest accuracy (AR and TR) we performed an error analysis to check what type of mistakes the network was making. For AR, there were 5 misclassified images. Of these 4 were acquired from the apical parasternal long axis view (A full description of echocardiographic views is available in [1]). It is logical the network might miss these cases as there were very few AR images acquired from this view in the training set because AR measurements are typically taken from the apical 5 chamber view. However, operators at different clinics may have different preferences, leading to the discrepancy between our training and test sets. The last image was judged to have been misclassified by the labeler and correctly classified by the network.

There were 16 misclassified TR images. Of these misclassifications 13 images were from the right ventricle inflow view. This view was not included in the training set because the labeler for the training set did not have experience with this view and thus ignored those images. Therefore, the network never had an opportunity to learn the pattern associated with these images. For one of the remaining images the class could not be determined during reanalysis, it was initially classified as TR because TR measurements were encoded in the file. The remaining 2 images were simply missed by the network.

C. Confidence Metric

To test the validity of the proposed confidence metric, we extracted the pre-softmax set of cutoff values on the training set and extracted quantile cutoff limits for each class from 0%-10% quantiles in 0.5% step sizes. The quantile is the ignored percentage on the training set: a quantile of 5% indicates that the 5% of images with the lowest pre-softmax values would be ignored.

We split the test set into two pieces, the first containing the 1422 correctly classified images (*correct* set) from E5 and the second containing the 57 misclassifications (*incorrect* set). The quantiles were used when running inference on these two sets of images as well as the full *test* set and the *unknown* and *extra* sets put aside during labeling. For each set, we iterated through the quantile values and recorded the ignored rate. For the test

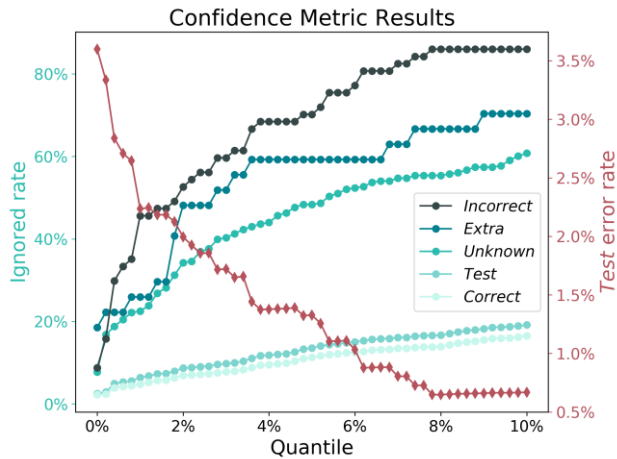


Fig. 8. Results of confidence metric experiments with ignored rates (green lines) on the left axis and error rate of the test set (red line) on the right axis. Ignored refers to the percentage of images which the network did not label because the output was beneath the cutoff for that quantile. *Test* refers to the test set of images. *Correct* is the subset of test images correctly classified by the network in E5 and *incorrect* is the subset of misclassifications. *Unknown* is the set of images which were unidentified during labeling. *Extra* is the set of images from classes not included in this network. An ideal confidence metric should completely ignore the *incorrect* and *extra* sets while ignoring none of the *correct* set. Ignoring the *unknown* set indicates the network accurately reflects expert confidence, but it is possible the network has detected features unseen to the observer.

set, the error rate was also recorded. Results are shown in Fig. 8, with ignored rates on the left axis and error rate on the right axis.

The confidence metric results may indicate some slight overfitting, and that the training and test sets came from different distributions. If the network is not overfit and the images are from the same distribution, the quantile should map 1:1 to the ignored test percentage. However, results showed at the 0.5% quantile 5% of the test images are ignored. A difference in distribution is expected given that the images came from separate clinics and matches what we found in our error analysis.

Results also demonstrated that our confidence metric accurately detected which images came from outside our training distribution and eliminated misclassified images at a much higher rate than correctly classified ones. For example, a user setting the confidence threshold at the 8% quantile mark would have to manually label 16% of their images but would achieve an accuracy of 99.5% on those images automatically classified because over 80% of the *incorrect* images would be ignored.

Both of the *unknown* and *extra* image sets were also ignored at a much higher rate, confirming that the metric identified out of distribution samples. For all three of the *incorrect*, *unknown*, and *extra* sets there was a sharp jump in the first quantile with >20% of images ignored at the 0.5% quantile. After this, ignored rates showed an approximately logarithmic relationship with increasing quantile values.

To validate our approach, we compared to several other methods of determining confidence. We implemented a MC-dropout [15] version of our model following the approach in

[27], where 50% of the neurons from the last fully connected layer were randomly dropped during each inference run. Each MC-dropout model was run 100 times, and we set quantile limits for values from the pre-softmax layer and softmax layer of the normal model, and from the mean and variance of the pre-softmax and softmax layers from the MC-dropout model. Results were similar for all implementations, with a slightly higher ignored rate for all sets when using the pre-softmax layer from either model. These results indicate that the choice of how to extract quantile values does not play a large role in the resulting confidence metric. The advantages of using the pre-softmax values are that it is simple to implement, and no additional experiments need to be run.

D. Implementation Details

All parameters were extracted automatically from private Dicom tags using Python 3.6. All pre-processing, training, and testing were carried out on Ubuntu machines with Python 3.6, PyTorch 0.4, and an NVIDIA Titan X GPU. The validation set was used to evaluate during preliminary experiments, but all networks were retrained using both the training and validation sets before they were evaluated with the final test set. We used normalization to center our dataset during training and inference. The heatmaps were already in the range [0, 1] because they are probability maps, so the B-mode images were also normalized to [0,1], then both images and heatmaps were mean-centered by subtracting the mean value of all pixels in all images in the training set. This value was 0.3 for the B-mode image and 0.0062 for the heatmap image.

IV. DISCUSSION

Our results indicate that highly accurate Doppler measurement type classification is possible in echocardiography *without* using the spectrum data. Accurate classification despite the omission of the Doppler spectra proves the network is learning the relationship between user input and anatomical structures. The spectrum data can be ignored because each class in our training (after using the mapping scheme) correlates to a unique physical location within the heart. Note that since each Doppler spectrum can be acquired from a variety of different views, this does not imply each class corresponds to a unique location in the input image, so accurate classification requires understanding of both the B-mode image and the cursor location. Highly accurate results have already been achieved on view recognition tasks in echocardiography (e.g. [7], [8]) indicating effective understanding of the B-mode image through CNNs. Our results take this a step farther. We show heatmaps are an effective way to encode physical location information into CNNs, demonstrating the ability to connect anatomical structural information (B-mode image) to relevant user input (Doppler cursor location) in a classification.

Since deep-learning algorithms deployed in clinical settings must frequently compete for resources, we analyzed how to decrease resource utilization. We demonstrated that a multi-head classification could reduce the memory footprint when the classification task can be split into separate problems by external parameters. The multi-head network (E5) was able to

maintain similar accuracy levels to those achieved by separate networks (E2) and much higher accuracy than a single network trained with all classes (E3). Our implementation achieved sub-5ms inference time, indicating near real-time performance.

We also conducted an error analysis of the mistakes made by the network. Encouragingly, the error analysis showed the network is accurately learning the image and heatmap patterns included during training. The errors seen were mostly from a mismatch between the training and test sets (including a mismatch between the labelers). Because the network accurately learned the patterns it was exposed to, we should be able to continually improve the accuracy by gathering additional training data that covers those cases it misclassified.

Misclassifications can be costly in a medical setting. It can lead to confusion when analyzing patient data and mistrust in artificial intelligence-based tools. To attempt to reduce misclassifications, we took several measures. First, we included a No Organ (NO) class in the training dataset to avoid classifying images of air and gel into another class. Second, we analyzed the training set output values from the last fully connected (“pre-softmax”) layer for each class and set cutoff limits. Images with a score below the cutoff were discarded rather than classified. Overall, results indicated that the proposed confidence metric can significantly reduce the error rate of the network by ignoring missed images in the test set at a much higher rate than correctly classified ones. The confidence metric also ignores the *unknown* and *extra* image sets at an approximately three times higher rate than those from the test set. Our method demonstrates one way to handle inputs from unseen distributions in a classification problem. Moreover, this implementation allows a user to easily set the quantile limit depending on the desired tradeoff between the error and ignored rates.

In future work, we hope to extend this method to public Dicom data (and thus multi-vendor). This is much easier because we don’t use the Doppler spectra in our pipeline; the B-mode image, Doppler cursor location, mode, and baseline are the only data needed. Although we extracted this information from raw data in the present work, all of it is also available from public Dicom tools and thus could be extracted from any vendor’s Doppler data. The main difference is there is some overlay on the publicly available B-mode image, potentially including color-flow. However, with a little effort we anticipate the ability to overcome this challenge and make our method fully multi-vendor.

V. CONCLUSION

In this work, we demonstrated a CNN-based method for the automated classification of Doppler measurement types. We showed notable performance gain on the task by encoding the Doppler cursor as a heatmap and appending it as a channel to the input and introducing a post-processing mapping scheme to simplify the problem. These methods would also be applicable to other tasks including location information as an input parameter and/or with linearly separable classes. We design a confidence metric capable of discarding a large proportion of images with high uncertainty to create a more reliable

classification system. Our method performs fast and accurate classification of Doppler measurement types. In the same way automatic echocardiographic view recognition unlocked fully automated processing of many B-mode images, our work unlocks fully automated Doppler spectra analysis, bringing increased efficiency and statistical power to clinical workflows.

REFERENCES

- [1] C. Mitchell *et al.*, “Guidelines for Performing a Comprehensive Transthoracic Echocardiographic Examination in Adults: Recommendations from the American Society of Echocardiography,” *J. Am. Soc. Echocardiogr.*, vol. 32, no. 1, pp. 1–64, 2019.
- [2] A. Alfirevic, “Back to the Future—Importance of Spectral Doppler,” *J. Cardiothorac. Vasc. Anesth.*, vol. 33, no. 5, pp. 1467–1470, 2018.
- [3] L. Mo, D. Becker, K. McCann, M. Honda, and S. Ishiguro, “Method and Apparatus for Automatic Tracing of Doppler Time-Velocity Waveform Envelope,” 5,935,074, 1999.
- [4] U. Lempertz and E. Sokulin, “Cardiac Auto Doppler White Paper,” 2017.
- [5] L. Deng *et al.*, “Recent advances in deep learning for speech research at Microsoft,” *ICASSP, IEEE Int. Conf. Acoust. Speech Signal Process. - Proc.*, pp. 8604–8608, 2013.
- [6] I. A. Wright, N. A. J. Gough, F. Rakebrandts, M. Wahabs, and J. P. Woodcock, “Neural network analysis of blood flow Doppler ultrasound signals: a pilot study,” *Eur. J. Ultrasound*, vol. 6, no. 5, p. S11, 2004.
- [7] A. Madani, R. Arnaout, M. Mofrad, and R. Arnaout, “Fast and accurate view classification of echocardiograms using deep learning,” *npj Digit. Med.*, vol. 1, no. 1, p. 6, Dec. 2018.
- [8] J. Zhang *et al.*, “Fully Automated Echocardiogram Interpretation in Clinical Practice,” *Circulation*, vol. 138, no. 16, pp. 1623–1635, 2018.
- [9] J. Ngiam, A. Khosla, and M. Kim, “Multimodal deep learning,” *... Mach. Learn. (...*, pp. 1–9, 2011.
- [10] A. Ephrat *et al.*, “Looking to Listen at the Cocktail Party: A Speaker-Independent Audio-Visual Model for Speech Separation,” vol. 37, no. 4, 2018.
- [11] G. Litjens *et al.*, “A Survey on Deep Learning in Medical Image Analysis.”
- [12] N. Tajbakhsh *et al.*, “Convolutional Neural Networks for Medical Image Analysis: Full Training or Fine Tuning?,” *IEEE Trans. Med. Imaging*, vol. 35, no. 5, pp. 1299–1312, 2016.
- [13] S. Falkner, A. Klein, and F. Hutter, “BOHB: Robust and Efficient Hyperparameter Optimization at Scale,” 2018.
- [14] Yarin Gal, “Uncertainty in Deep Learning,” *phd thesis*, vol. 1, no. 1, pp. 1–11, 2017.
- [15] Y. Gal and G. Zoubin, “Dropout as a Bayesian Approximation: Representing Model Uncertainty in Deep Learning,” in *international conference on machine learning*, 2016, pp. 1050–1059.
- [16] C. Guo, G. Pleiss, Y. Sun, and K. Q. Weinberger, “On Calibration of Modern Neural Networks,” 2017.
- [17] B. Zadrozny and C. Elkan, “Transforming classifier scores into accurate multiclass probability estimates,” 2004, p. 694.
- [18] N. B. Schiller *et al.*, “Recommendations for Quantitation of the Left Ventricle by Two-Dimensional Echocardiography,” *J. Am. Soc. Echocardiogr.*, vol. 2, no. 5, pp. 358–367, 1989.
- [19] K. K. Kadappa and L. Thomas, “Tissue doppler imaging in echocardiography: Value and limitations,” *Hear. Lung Circ.*, vol. 24, no. 3, pp. 224–233, 2015.
- [20] R. Liu *et al.*, “An Intriguing Failing of Convolutional Neural Networks and the CoordConv Solution,” 2018.
- [21] A. Nibali, Z. He, S. Morgan, and L. Prendergast, “Numerical Coordinate Regression with Convolutional Neural Networks,” no. January, 2018.
- [22] S. Ruder, “An Overview of Multi-Task Learning in Deep Neural Networks,” 2017.
- [23] S. Bianco, R. Cadene, L. Celona, and P. Napoletano, “Benchmark Analysis of Representative Deep Neural Network Architectures,” *IEEE Access*, vol. 6, 2018.

- [24] X. Zhang, S. Ren, and J. Sun, "Deep Residual Learning for Image Recognition," in *Proceedings of the IEEE conference on computer vision and pattern recognition*, 2016.
- [25] F. N. Iandola, S. Han, M. W. Moskewicz, K. Ashraf, W. J. Dally, and K. Keutzer, "SqueezeNet: AlexNet-level accuracy with 50x fewer parameters and <0.5MB model size," pp. 1–13, 2016.
- [26] M. Sandler, A. Howard, M. Zhu, A. Zhmoginov, and L. C. Chen, "MobileNetV2: Inverted Residuals and Linear Bottlenecks," *Proc. IEEE Comput. Soc. Conf. Comput. Vis. Pattern Recognit.*, pp. 4510–4520, 2018.
- [27] Y. Geifman and R. El-Yaniv, "Selective Classification for Deep Neural Networks," no. Nips, 2017.